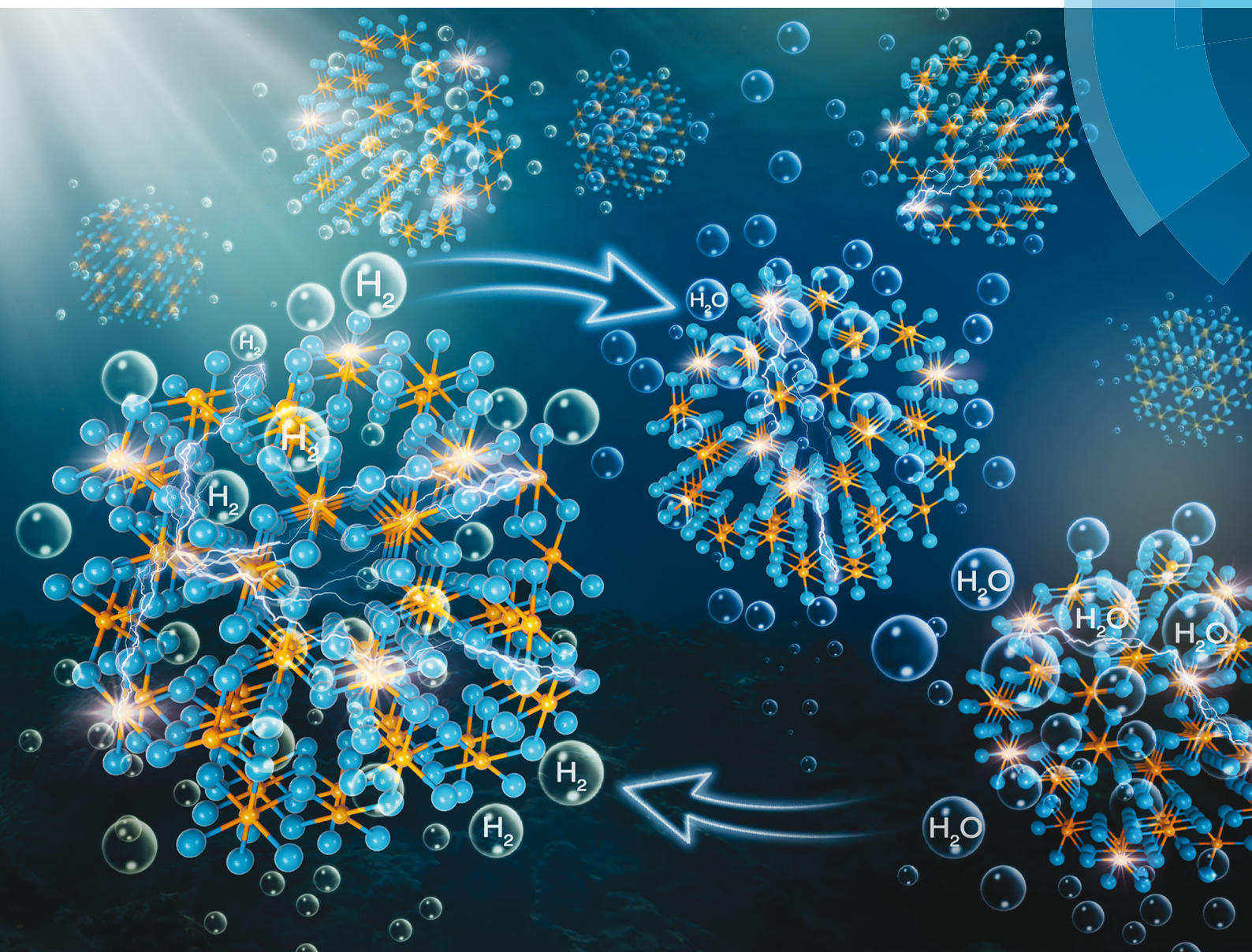


Energy & Environmental Science

rsc.li/ees



ISSN 1754-5706



ROYAL SOCIETY
OF CHEMISTRY

Celebrating
IYPT 2019

PAPER

Tao Cheng, Yanguang Li et al.

Weakening hydrogen adsorption on nickel via interstitial nitrogen doping promotes bifunctional hydrogen electrocatalysis in alkaline solution



Cite this: *Energy Environ. Sci.*, 2019, 12, 3522

Weakening hydrogen adsorption on nickel via interstitial nitrogen doping promotes bifunctional hydrogen electrocatalysis in alkaline solution[†]

Tingting Wang,^{†,a} Miao Wang,^{‡,a} Hao Yang,^{‡,a} Mingquan Xu,^b Chuandong Zuo,^c Kun Feng,^a Miao Xie,^a Jun Deng,^a Jun Zhong,^{id,a} Wu Zhou,^b Tao Cheng^{id,*a} and Yanguang Li^{id,*a}

Ni-Based materials are promising candidates for the electrocatalytic hydrogen oxidation reaction and hydrogen evolution reaction in alkaline solution. However, pure Ni binds hydrogen very strongly. To promote its electrocatalytic activity would require the weakening of its hydrogen binding energy. Here, we demonstrate that interstitial nitrogen doping in Ni_3N can greatly promote its electrocatalytic activity. Ni_3N nanoparticles are prepared from the controlled nitridation of Ni-based coordination polymer nanosheets. The resultant product exhibits excellent mass activity superior to most existing non-precious-metal-based materials and great CO-tolerance for the hydrogen oxidation reaction, as well as remarkable activity and stability for the hydrogen evolution reaction. Our experimental results are further understood and supported by theoretical simulations showing that the interstitial nitrogen doping significantly decreases the hydrogen binding energy and lowers the activation barrier for water formation and dissociation.

Received 30th May 2019,
Accepted 28th August 2019

DOI: 10.1039/c9ee01743g

rsc.li/ees

Broader context

The development of efficient non-precious-metal-based electrocatalysts for the bifunctional hydrogen oxidation reaction and hydrogen evolution reaction in alkaline solution is important to the commercial success of low-cost alkaline fuel cells and alkaline water electrolyzers, but it is very challenging. Ni-Based materials are promising candidates and in fact the only non-precious-metal-based candidates for hydrogen oxidation. Unfortunately, pure Ni metal has relatively strong hydrogen adsorption, which essentially limits its electrocatalytic performance. In this work, we show that the interstitial nitrogen doping of Ni metal represents an effective strategy to weaken its hydrogen adsorption. Ni_3N nanoparticles prepared from the controlled nitridation of Ni-based coordination polymer nanosheets demonstrate excellent activity, high stability, and CO-tolerance in alkaline solution superior to most non-precious-metal-based materials. Our experimental results are further understood and supported by theoretical simulations.

Introduction

Hydrogen has been widely advocated as the ideal energy carrier for the future by virtue of its high energy density and

environmental friendliness.¹ Its electrochemical utilization can be realized through two key reactions, *i.e.*, the hydrogen oxidation reaction (HOR) and the hydrogen evolution reaction (HER).² The former is the anodic process in fuel cells that transforms chemical energy into electricity, while the latter takes place during water splitting that stores electrical energy in the form of chemical bonds. Pt and its alloys have been the most active electrocatalysts so far for the HOR/HER, but their commercial viability is severely undermined by their high costs.^{3–6} On the other hand, recent interest in alkaline fuel cells and alkaline water electrolyzers calls for the development of efficient HOR/HER electrocatalysts in alkaline solution.^{5–8} Studies reveal that the reaction kinetics of both HOR and HER on Pt is two to three orders of magnitude lower in alkaline solution compared to that in acidic solution, leaving much room for improvement.^{9,10} There is a pressing need to develop

^a Institute of Functional Nano and Soft Materials (FUNSOM), Jiangsu Key Laboratory for Carbon-Based Functional Materials and Devices, Soochow University, Suzhou 215123, China. E-mail: tcheng@suda.edu.cn, yanguang@suda.edu.cn

^b School of Physical Sciences, University of Chinese Academy of Sciences, Beijing, 100049, China

^c Beijing Key Laboratory of Opto-Electronic Functional Materials & Micro-Nano Devices, Department of Physics, Renmin University of China, Beijing, 100872, China

[†] Electronic supplementary information (ESI) available. See DOI: 10.1039/c9ee01743g

[‡] These authors contributed equally to this work.

non-precious-metal-based electrocatalysts with activity on a par with or even exceeding that of Pt in alkaline solution. In particular, the development of bifunctional hydrogen electrocatalysts is highly desirable for unitized regenerative fuel cells that can work and switch between the fuel cell mode and water electrolyzer mode to enable reversible hydrogen generation and utilization.¹¹

There are a number of reports about non-precious-metal-based materials for the HER in alkaline solution.^{7,12–14} Some of them approach the activity of Pt. By contrast, much less attention is paid on the HOR. Ni-Based materials are the only non-precious-metal-based candidates having decent HOR activities in base.^{5,6} Unfortunately, pure Ni metal has relatively strong *H adsorption. Its Gibbs free energy for hydrogen adsorption (ΔG_{H^*} , which is a key descriptor for both HOR and HER) was calculated to be ~ -0.3 eV—some distance away from the thermoneutral point ($\Delta G_{H^*} = 0$).¹⁵ To further promote its HOR/HER activity would require considerably weakening its H adsorption. In the literature, this is achieved by alloying Ni with different metals such as Cr, Mo, Co, Fe, Cu and Ti.^{16–20} For example, Yan and coworkers reported that ternary metallic CoNiMo from electrodeposition had an H binding energy similar to Pt and much lower than Ni, and therefore exhibited a specific HOR activity ~ 20 times higher than that of Ni in alkaline solution.¹⁸ In addition, the synergistic effort between the catalyst and support is explored to modify the electronic

structure of Ni and improve its electrocatalytic activity.²¹ Despite these exciting advances, the HOR activities of Ni-based electrocatalysts are still insufficient to render them practically viable.

In this work, we report that the interstitial N doping of Ni metal is an effective strategy to weaken its H adsorption and consequently to promote its bifunctional HOR/HER activity. Ni_3N nanoparticles are prepared from the controlled nitridization of a Ni-based cyano-bridged coordination polymer in NH_3 . The resultant product demonstrates excellent activity, high stability, and CO-tolerance in alkaline solution superior to most non-precious-metal-based materials. Our experimental results are further understood and supported by theoretical simulations.

Results and discussion

We developed a facile two-step synthetic method to prepare Ni_3N nanoparticles as schematically illustrated in Fig. 1a. In the first step, $\text{K}_2[\text{Ni}(\text{CN})_4]$ was reacted with $\text{Ni}(\text{NO}_3)_2$ in solution in the presence of polyvinylpyrrolidone (PVP), giving rise to a solid precipitate with a light cyan color (see Experimental methods for details). The X-ray diffraction (XRD) pattern of the precipitate exhibits diffraction peaks resembling those of a dehydrated Hofmann-type coordination polymer, in which adjacent transition metal atoms are bridged together by cyano groups (Fig. S1, ESI†).²²

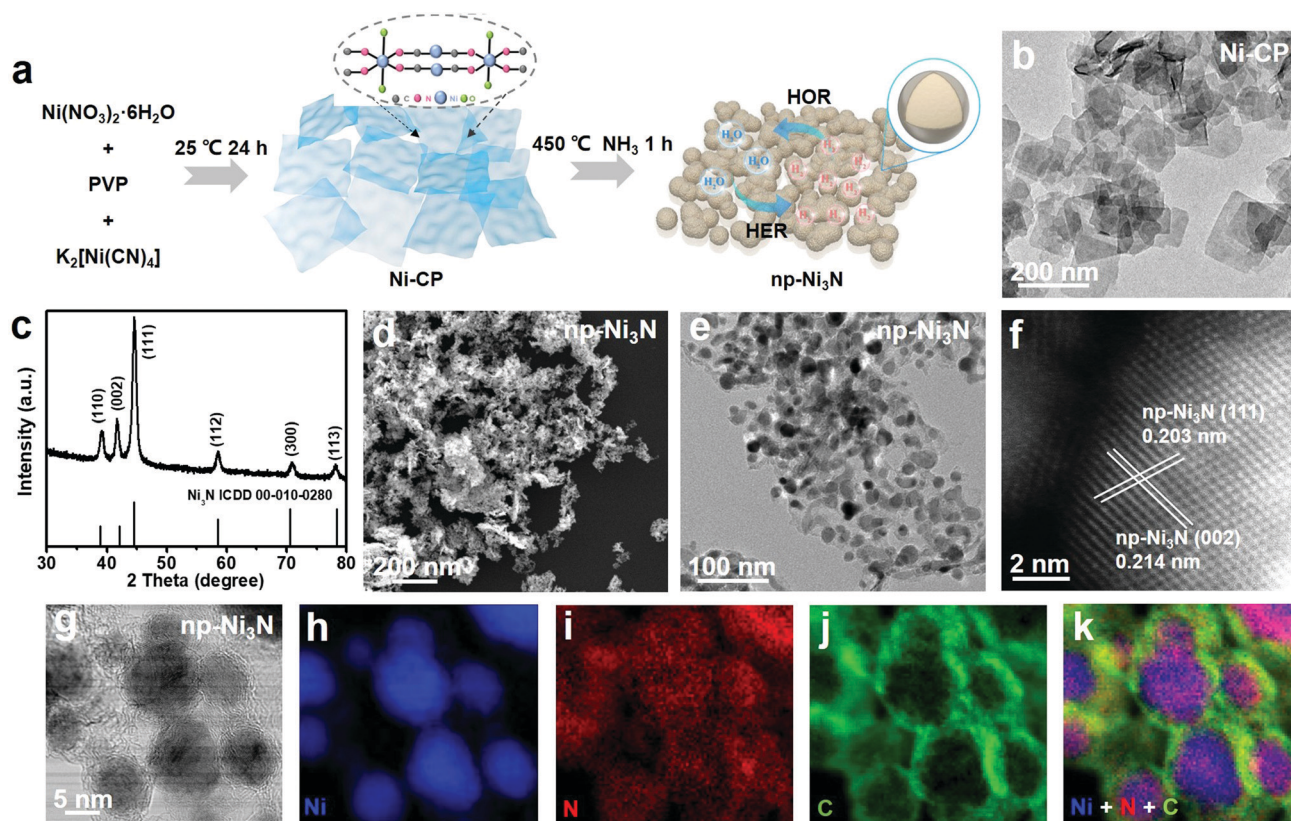


Fig. 1 Preparation and structural characterization of np- Ni_3N . (a) Schematic synthetic procedure toward np- Ni_3N ; (b) TEM image of Ni-CP; (c) XRD pattern, (d) SEM image, (e) TEM image and (f and g) STEM images of np- Ni_3N ; (h–k) elemental mapping of Ni, N and C.

It is named Ni-CP for short. From transmission electron microscopy (TEM) images, Ni-CP is revealed to consist of roughly square nanosheets (Fig. 1b). Their lateral size is measured to be 100–200 nm. Importantly, we find that the introduction of PVP is critical to the formation of Ni-CP nanosheets presumably *via* selectively passivating the basal plane. A small amount of PVP remains adsorbed on the Ni-CP surface even after extensive washing as reflected by its characteristic signals from Fourier-transform infrared spectroscopy (FT-IR) (Fig. S2, ESI[†]). Only microsized irregular particles result in the absence of PVP under otherwise identical conditions.

For the second step, Ni-CP was nitridized under NH₃ at 450 °C. The precise control of the nitridization temperature is the decisive key here since Ni-CP cannot be fully converted at lower temperatures (<400 °C), whereas interstitial N dopants start to escape from the lattice and metallic Ni starts to emerge at higher temperatures (>450 °C). XRD analysis in Fig. 1c evidences that the final product is composed of hexagonal Ni₃N (JCPDS card No. 10-0280). Its average particle size is estimated to be ~12 nm from the (111) peak width according to the Scherrer formula. Of important note, the XRD pattern of Ni₃N appears very similar to that of hexagonal Ni metal. Care should be taken to distinguish these two different phases. Scanning electron microscopy (SEM) examination shows that the original Ni-CP nanosheets are transformed into nanoparticles after the nitridization (Fig. 1d). The final product is therefore named np-Ni₃N. The size of these nanoparticles is measured to be in the range of 5–20 nm from the TEM image

(Fig. 1e), in reasonably good agreement with the XRD analysis result above. They are embedded in a partially graphitic network, which is believed to be derived from the carbonization of surface-adsorbed PVP. This is supported by the thermogravimetric analysis (TGA) of PVP alone under N₂ showing that it is mostly carbonized at 450 °C (Fig. S3, ESI[†]). Our control experiment also indicates that when the material is prepared in the absence of PVP, the final annealing product is completely free of the carbonaceous network (Fig. S4, ESI[†]). The high-resolution TEM image of Ni₃N nanoparticles unveils clear lattice fringes assignable to the (111) and (002) planes (Fig. 1f). Moreover, energy dispersive spectroscopy (EDS) elemental mapping of Ni, N, and C was carried out with scanning transmission electron microscopy (STEM) (Fig. 1g–k). Comparison of their spatial distribution leads us to conclude that each Ni₃N nanoparticle contains abundant interstitial N dopants and that the carbonaceous network is also doped with N. An additional set of EDS mapping results is available in Fig. S5 (ESI[†]). The weight percentage of Ni₃N nanoparticles in the final product is estimated to be 71.7 wt% from its TGA in the air (Fig. S6, ESI[†]). For the purpose of comparison, Ni-CP was also annealed in Ar at 450 °C for the second step. The resultant product has a similar nanoparticle morphology but is mainly composed of Ni (Fig. S7, ESI[†]). It is named np-Ni for short.

To probe the bonding state and chemical environment of np-Ni₃N, we further conducted X-ray photoelectron spectroscopy (XPS) and X-ray absorption spectrum (XAS) analysis. The Ni 2p_{3/2} XPS spectrum exhibits the Ni-N signal (at 852.7 eV) from Ni₃N

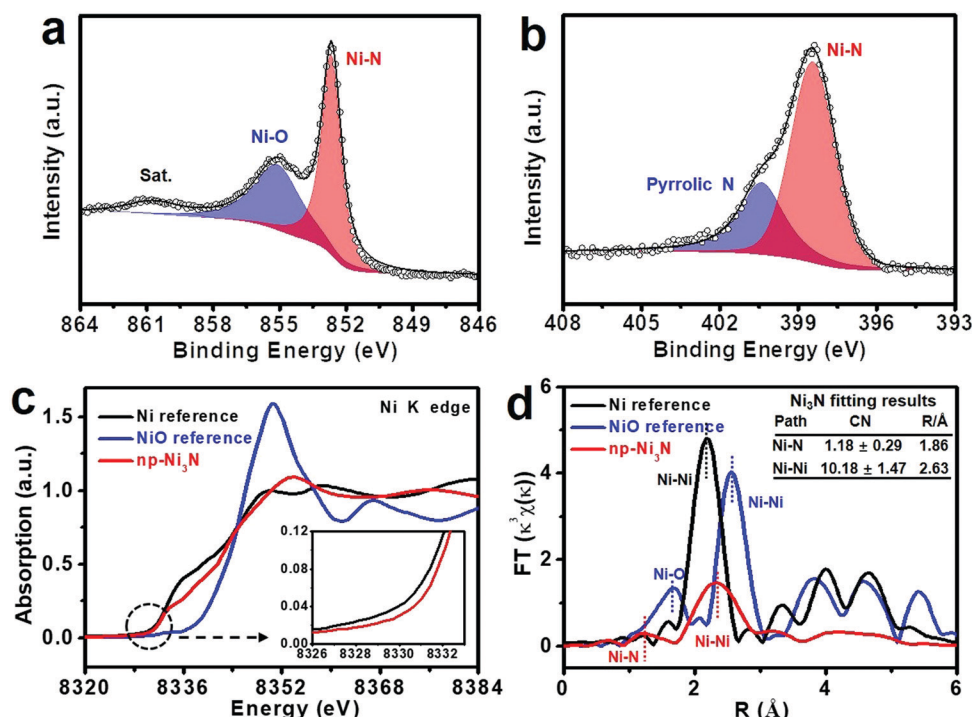


Fig. 2 Spectroscopic characterization of np-Ni₃N. (a and b) High-resolution Ni 2p and N 1s XPS spectra of np-Ni₃N with appropriate peak deconvolution; (c) Ni K-edge XANES spectrum of np-Ni₃N in comparison with the Ni and NiO references; the inset is an enlarged image of the circled area in (c); (d) EXAFS spectrum of np-Ni₃N in comparison with the Ni and NiO references; the inset shows the fitting results for np-Ni₃N.

and the Ni–O signal (at 855.2 eV) from its superficial oxide layer (Fig. 2a).^{23,24} Deconvolution of the N 1s XPS spectrum also reveals the contribution of Ni–N (at 398.3 eV) probably overlaid with pyridinic N as well as the contribution of pyrrolic N (at 400.3 eV) from the carbonaceous network (Fig. 2b).^{23,24} From the Ni K-edge X-ray adsorption near-edge structure (XANES) spectrum, the adsorption edge of Ni₃N locates very close to that of the Ni foil, and under careful scrutiny, it is observed to be slightly shifted toward higher energy from the reference (Fig. 2c). This indicates that Ni in Ni₃N resembles its metallic state but carries a partial positive charge. Fig. 2d shows the extended X-ray absorption fine structure (XANES) from the Fourier transform of Fig. 2c. Compared to the Ni foil reference, the main peak of np-Ni noticeably shifts to the right, evidencing that the Ni–Ni bond length is slightly elongated upon N incorporation.^{25,26} Its minor shoulder at 1.89 Å signals the Ni–N bonding. Fitting the spectrum yields a Ni–N coordination number (CN) of 1.18 ± 0.29 , and a Ni–Ni CN of 10.18 ± 1.47 , smaller than the expected values (2 and 12, respectively) for bulk Ni₃N. This can be rationalized by the nanoscale particle size. The interstitial N doping is also probably off stoichiometry. By contrast, EXAFS of np-Ni shows a Ni–Ni peak position similar to that of the Ni foil in spite of the much-decreased peak intensity (Fig. S8, ESI†).

Next, we investigated the electrocatalytic performance of np-Ni₃N for the HOR in 0.1 M KOH (see Experimental methods for details). The catalyst was uniformly cast onto a glassy carbon rotating disk electrode (RDE) to achieve an active material (*i.e.* Ni₃N) loading of 0.16 mg cm^{-2} . All the potential readings here are reported on the reversible hydrogen electrode (RHE)

scale and compensated for the ohmic loss. When the electrolyte is saturated with Ar, a negligible anodic current density is measured (Fig. S9, ESI†). When the electrolyte is saturated with H₂, np-Ni exhibits a very low HOR activity, whereas the anodic current density of np-Ni₃N takes off at $\sim 0 \text{ V}$ and rises significantly with increasing overpotential (Fig. 3a). The current density of np-Ni₃N reaches $\sim 1.7 \text{ mA cm}^{-2}$ at $\eta = 50 \text{ mV}$ and an electrode rotation speed of 1600 rpm. To our best knowledge, this is the highest attainable value among all Ni-based HOR electrocatalysts under equivalent conditions,^{17,21,27,28} and it approaches those of the 20 wt% Pt/C benchmark ($\sim 1.85 \text{ mA cm}^{-2}$, at a loading of $10 \mu\text{g}_{\text{Pt}} \text{ cm}^{-2}$) and 20 wt% PtRu/C benchmark ($\sim 2.43 \text{ mA cm}^{-2}$, at a loading of $10 \mu\text{g}_{\text{Pt+Ru}} \text{ cm}^{-2}$). One advantage of using non-precious-metal-based electrocatalysts is their low cost. Despite their inferior specific activity, one can increase the catalyst loading to achieve an apparent activity comparable or even superior to those of the precious metal benchmarks. Here, when the loading of Ni₃N is doubled ($\sim 0.32 \text{ mg cm}^{-2}$), the HOR current density is increased to be 2.2 mA cm^{-2} at $\eta = 50 \text{ mV}$, and reaches the diffusion limit ($\sim 2.8 \text{ mA cm}^{-2}$) at $\eta = 100 \text{ mV}$. Its current density at $\eta = 50 \text{ mV}$ is superior to that of 20 wt% Pt/C and close to that of 20 wt% PtRu/C. The above results clearly highlight the great potential of our np-Ni₃N for the HOR in alkaline solution. Further increasing the catalyst loading doesn't result in additional performance gain (Fig. S10, ESI†). Moreover, in order to reveal the nature of electrochemically active species, np-Ni₃N is dispersed in 0.5 M HCl under continuous magnetic stirring overnight to selectively remove Ni₃N nanoparticles (Fig. S11, ESI†).

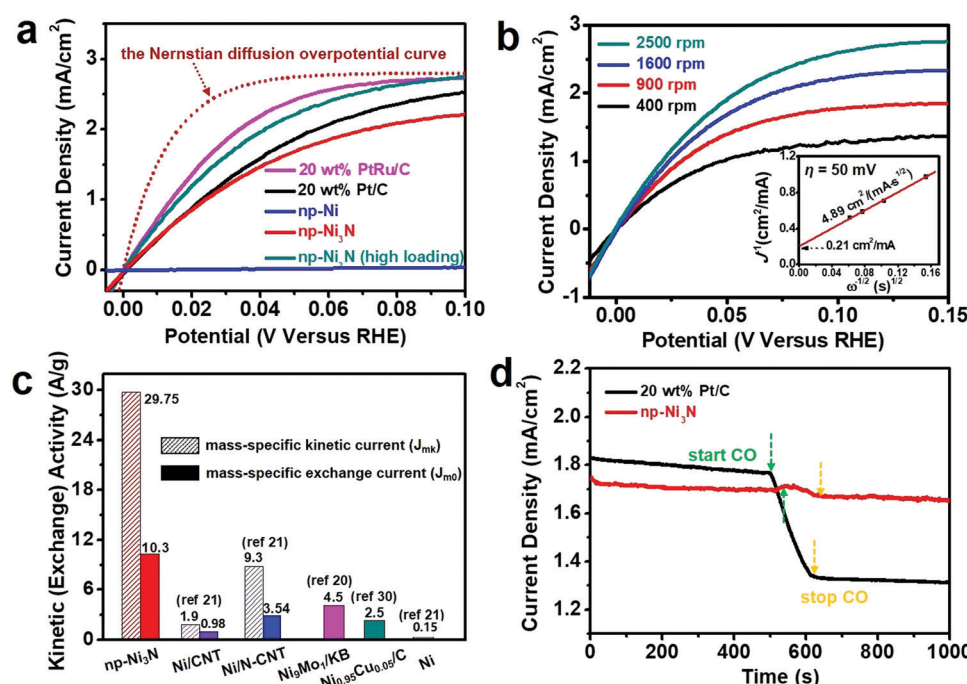


Fig. 3 HOR performance of Ni₃N in 0.1 M KOH. (a) HOR polarization curves of np-Ni, np-Ni₃N, 20 wt% Pt/C and 20 wt% PtRu/C; the dotted red line represents the Nernstian diffusion overpotential curve; (b) polarization curves of np-Ni₃N at different electrode rotation speeds; the inset is the corresponding Koutecky–Levich plot at $\eta = 50 \text{ mV}$; (c) comparison of the mass-specific activity of mp-Ni₃N with previous results reported in the literature; (d) CO poisoning experiments of np-Ni₃N and 20 wt% Pt/C.

The electrochemical measurement of the catalyst after the acid leaching reveals a negligible HOR activity. This evidences that Ni_3N rather than the N-doped carbonaceous network is HOR-active.

Further, the mass-specific activity of np- Ni_3N was calculated. Fig. 3b depicts the RDE polarization curves at different electrode rotation speeds from 400 rpm to 2500 rpm. As dictated by the Koutecky-Levich equation, a linear correlation is obtained by plotting the reciprocal current density (J^{-1}) at $\eta = 50$ mV with respect to the square root of reciprocal rotation speed ($\omega^{-1/2}$) (inset of Fig. 3b). The kinetic current density (J_k) is derived from the extrapolation of the linear correlation to $\omega^{-1/2} = 0$ and is calculated to be 4.76 mA cm^{-2} at $\eta = 50$ mV. The corresponding mass-specific kinetic current (J_{mk}) is then estimated to be 29.8 A g^{-1} for np- Ni_3N (Method 1, ESI†). Moreover, the mass-specific exchange current (J_{mo}) is also determined from the linear fitting of the micro-polarization region around the equilibrium potential and is calculated to be 10.3 A g^{-1} for np- Ni_3N (Method 2, ESI†). Remarkably, we find that both J_{mk} and J_{mo} of our np- Ni_3N are significantly improved over all previous Ni-based HOR electrocatalysts as summarized in Fig. 3c and Table S1 (ESI†).^{17,21,27,29,30} For example, as one of the best candidates previously reported, Ni nanoparticles supported on N-doped carbon nanotubes (Ni/N-CNT) only had $J_{mk} = 9.3 \text{ A g}^{-1}$ at $\eta = 50$ mV and $J_{mo} = 3.54 \text{ A g}^{-1}$.²¹ It is worth mentioning that we don't pursue the electrochemical surface area (ECSA) of Ni_3N and consequently the ECSA-normalized kinetic current due to the large uncertainty associated with this practice.

Other than high activity, CO tolerance is another important consideration in the pursuit of future HOR electrocatalysts.³¹ This is because at present the majority of H_2 is produced from natural gas reforming, which unavoidably introduces CO to the fuel stream for fuel cell applications. Pt is known for its high vulnerability to CO poisoning even at low levels (~ 10 ppm), resulting in marked performance degradation.^{32,33} Here, the CO tolerance of our electrocatalyst was assessed by feeding diluted (5%) CO to the electrolyte for a short period (~ 100 s) during the chronoamperometric measurement at $\eta = 50$ mV. As we can see from Fig. 3d, the anodic current density of Pt abruptly drops from $\sim 1.8 \text{ mA cm}^{-2}$ to $\sim 1.3 \text{ mA cm}^{-2}$ in the

presence of CO, and cannot be recovered even when the fuel stream is reverted to pure H_2 . By stark contrast, the introduction of CO has a negligible influence on the activity of np- Ni_3N , and its current density is maintained at $\sim 1.7 \text{ mA cm}^{-2}$. This observation unambiguously underscores the great CO-tolerance of np- Ni_3N as the HOR electrocatalyst.

Having established the great HOR performance of np- Ni_3N , we went on to examine its HER activity on the RDE in alkaline solution. Ni-Based materials are widely investigated as HER electrocatalysts, but few of them have an activity comparable to the Pt benchmark.¹³ For this part of the study, the electrolyte in use was 1 M KOH for its higher ionic conductivity and to allow direct comparison with literature results. As depicted in Fig. 4a, the np- Ni_3N electrode with an active material loading of 0.16 mg cm^{-2} exhibits a virtually zero onset overpotential. Its cathodic current density rapidly increases beyond the onset and requires only 68 mV to deliver $J = 10 \text{ mA cm}^{-2}$. This overpotential is just slightly larger than that of 20 wt% Pt/C ($\eta_{10 \text{ mA cm}^{-2}} = 61 \text{ mV}$, at a loading of $10 \mu\text{g}_{\text{Pt}} \text{ cm}^{-2}$) and 20 wt% PtRu/C ($\eta_{10 \text{ mA cm}^{-2}} = 40 \text{ mV}$, at a loading of $10 \mu\text{g}_{\text{Pt+Ru}} \text{ cm}^{-2}$) and considerably improved compared to np-Ni ($\eta_{10 \text{ mA cm}^{-2}} = 248 \text{ mV}$) as well as other non-precious-metal-based HER electrocatalysts (Table S2, ESI†).^{34–36} Doubling the electrocatalyst loading (0.32 mg cm^{-2}) further reduces the overpotential to $\eta_{10 \text{ mA cm}^{-2}} = 50 \text{ mV}$. As far as we are aware, this represents the highest HER activity ever reported in alkaline solution under comparable catalyst loading (Table S2, ESI†). Furthermore, the electrocatalyst stability is assessed by chronopotentiometry ($i \sim t$) measurements at a constant cathodic current density of 10 mA cm^{-2} (Fig. 4b). np- Ni_3N exhibits great HER stability with negligible overpotential increase. At the end of the 1500 s measurement, its activity already surpasses that of the Pt benchmark. Longer stability tests are appealing but restricted on the RDE for safety consideration. Alternatively, np- Ni_3N is loaded on a carbon fiber paper electrode and demonstrated to have outstanding long-term chronopotentiometric stability ($> 10000 \text{ s}$) for the HER at 10 mA cm^{-2} and HOR at 5 mA cm^{-2} (Fig. S12, ESI†). Please note that the significantly larger HOR current density measured on carbon fiber paper than that measured on the RDE is due to the much facilitated H_2 diffusion through the carbon fiber paper current collector.

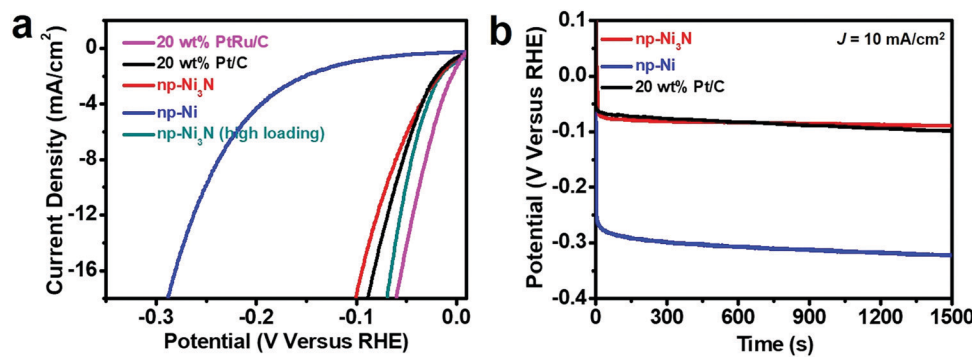


Fig. 4 HER performance of Ni_3N in 1 M KOH. (a) HER polarization curves of np-Ni, np- Ni_3N , 20 wt% Pt/C and 20 wt% PtRu/C; (b) chronoamperometric stability of np-Ni, np- Ni_3N and 20 wt% Pt/C for HER at 10 mA cm^{-2} .

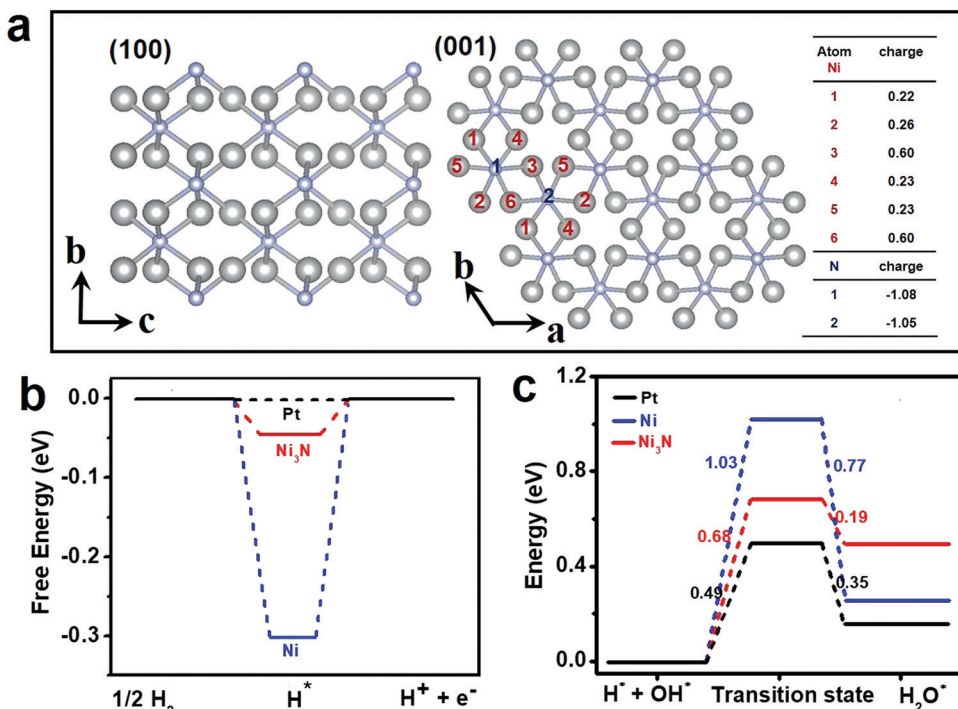


Fig. 5 DFT simulation of the HOR and HER processes on Ni₃N, Ni and Pt. (a) Atomic arrangements of (grey) Ni and (light blue) N on (left) the (100) plane and (right) the (001) plane of the Ni₃N crystal structure; the inset table highlights the calculated Bader charge on Ni and N, showing the charge separation between Ni and N; (b) Gibbs free energy for hydrogen adsorption (ΔG_{H^*}) on Ni₃N, Ni, and Pt; (c) energy barrier for water formation (from left to right) and water dissociation (from right to left) on Ni, Ni₃N, and Pt.

The above experiments conclude that the interstitial N doping in np-Ni₃N significantly promotes its bifunctional activity and stability for the HOR and HER in alkaline solution. In order to gain an in-depth understanding of the origin of the improvement, theoretical computations were conducted to simulate the HOR/HER process on Ni₃N as well as on Ni and Pt. Fig. 5a depicts the atomic arrangement of Ni and N atoms on the (100) and (001) planes (see Experimental methods for simulation details). The introduction of interstitial N dopants is found to oxidize Ni, which bears formal charges ranging from +0.22 to +0.60 based on the Bader charge analysis. Such a partial positive charge may greatly impact the binding energy of the reaction intermediates on the Ni surface.

Gibbs free energy for hydrogen adsorption (ΔG_{H^*}) is an important descriptor for both HOR and HER. According to the Sabatier principle, ideal HOR/HER electrocatalysts should have ΔG_{H^*} close to zero. Pure Ni metal has a relatively poor HOR/HER activity because it binds H very strongly. The ΔG_{H^*} value is calculated to be -0.30 eV on Ni(111) from our density functional theory (DFT) calculations, in line with previous studies.¹⁵ As for Ni₃N, the partial positive charge on the Ni site due to the presence of the interstitial N dopant significantly weakens the hydrogen adsorption and gives rise to $\Delta G_{H^*} = -0.05$ eV on the most favorable plane, very close to that of Pt (Fig. 5b).

Here, the calculation of ΔG_{H^*} doesn't take into consideration the pH effect. Even though the detailed reaction pathways in alkaline solution are still under debate, it becomes increasingly accepted that the alkaline HOR/HER is not entirely

controlled by ΔG_{H^*} .³⁷ Strong experimental evidence is given by Markovic and coworkers that the reaction between surface adsorbed *OH and H* to form H₂O is a key step of the HOR under alkaline conditions,³⁷ while the dissociative adsorption of H₂O to *OH and H* is the prerequisite for the alkaline HER.³⁸ The slow kinetics of these two processes directly contribute to the much lower HOR/HER activity of Pt in alkaline solution than in acidic solution. Considering this, we also simulated the process of water formation from and its dissociation to *OH and H* as shown in Fig. 5c and Fig. S13 (ESI†). The barrier height of water formation is calculated to be 1.03 eV for Ni, 0.68 eV for Ni₃N and 0.49 eV for Pt. The barrier height of water dissociation is calculated to be 0.77 eV for Ni, 0.19 eV for Ni₃N and 0.35 eV for Pt. These results indicate that the incorporation of interstitial N dopants significantly lowers the activation energy for both water formation and dissociation, and Ni₃N is an excellent HOR/HER electrocatalyst in alkaline solution.

Conclusion

In summary, we demonstrated that interstitial N doping in Ni₃N considerably weakened its H binding and greatly promoted its bifunctional activity for the HOR and HER in alkaline solution. Ni₃N nanoparticles were prepared from the controlled nitridization of Ni-based coordination polymer nanosheets. The final product consisted of 5–20 nm Ni₃N nanoparticles embedded in a partially graphitic network. When assessed as the HOR electrocatalyst, np-Ni₃N at low loading (0.16 mg cm⁻²) delivered an anodic

current density of $\sim 1.7 \text{ mA cm}^{-2}$ (at $\eta = 50 \text{ mV}$) on a RDE at 1600 rpm, a mass-specific kinetic current of 29.8 A g^{-1} (at $\eta = 50 \text{ mV}$), and a mass-specific exchange current of 10.3 A g^{-1} . All these metrics were superior to those of existing non-precious-metal-based electrocatalysts to our best knowledge. At high loading (0.32 mg cm^{-2}), its apparent HOR activity even exceeded that of 20 wt% Pt/C and closely approached that of 20 wt% PtRu/C. Ni₃N also exhibited impressive CO tolerance and operation stability. When assessed as the HER electrocatalyst, np-Ni₃N had virtually zero overpotential and required only 50–68 mV to achieve a cathodic current density of 10 mA cm^{-2} . These experimental results were understood by DFT calculations showing that the interstitial N doping in Ni₃N significantly decreased the H binding energy and at the same time lowered the activation barrier for water formation and dissociation. Our study represents a new approach toward the rational design of non-precious-metal-based bifunctional hydrogen electrocatalysts with performances approaching or superior to that of the precious metal benchmark.

Author contribution

Y. L. conceived the project and designed the experiments. T. W. and M. W. prepared the material and performed electrochemical measurements. H. Y., M. X. and T. C. conducted the theoretical calculations. M. X. and W. Z. performed the STEM imaging and EDS mapping. K. F. and J. Z. carried out XANES and EXAFS analysis. C. Z. assisted in the material preparation and electrochemical measurements. J. D. conducted regular TEM imaging.

Conflicts of interest

There are no conflicts to declare.

Acknowledgements

We acknowledge support from the Ministry of Science and Technology of China (2017YFA0204800), the Priority Academic Program Development of Jiangsu Higher Education Institutions and Collaborative Innovation Center of Suzhou Nano Science and Technology. We thank Dr Lu Ma from Argonne National Laboratory for fitting the EXAFS result.

References

- J. A. Turner, *Science*, 2004, **305**, 972–974.
- V. R. Stamenkovic, D. Strmcnik, P. P. Lopes and N. M. Markovic, *Nat. Mater.*, 2016, **16**, 57–69.
- Y. Zheng, Y. Jiao, M. Jaroniec and S. Z. Qiao, *Angew. Chem., Int. Ed.*, 2015, **54**, 52–65.
- P. C. K. Vesborg, B. Seger and I. Chorkendorff, *J. Phys. Chem. Lett.*, 2015, **6**, 951–957.
- E. S. Davydova, S. Mukerjee, F. Jaouen and D. R. Dekel, *ACS Catal.*, 2018, **8**, 6665–6690.
- Y. Cong, B. Yi and Y. Song, *Nano Energy*, 2018, **44**, 288–303.
- Y. Zheng, Y. Jiao, A. Vasileff and S. Z. Qiao, *Angew. Chem., Int. Ed.*, 2018, **57**, 7568–7579.
- N. Mahmood, Y. Yao, J. W. Zhang, L. Pan, X. Zhang and J. J. Zou, *Adv. Sci.*, 2018, **5**, 1700464.
- W. Sheng, H. A. Gasteiger and Y. Shao Horn, *J. Electrochem. Soc.*, 2010, **157**, B1529–B1536.
- W. Sheng, Z. Zhuang, M. Gao, J. Zheng, J. G. Chen and Y. Yan, *Nat. Commun.*, 2015, **6**, 5848.
- G. L. Soloveichik, *Proc. IEEE*, 2014, **102**, 964–975.
- X. Zou and Y. Zhang, *Chem. Soc. Rev.*, 2015, **44**, 5148–5180.
- M. Gong, D. Y. Wang, C. C. Chen, B. J. Hwang and H. Dai, *Nano Res.*, 2016, **9**, 28–46.
- M. Zeng and Y. Li, *J. Mater. Chem. A*, 2015, **3**, 14942–14962.
- J. K. Norskov, T. Bligaard, A. Logadottir, J. R. Kitchin, J. G. Chen, S. Pandelov and U. Stimming, *J. Electrochem. Soc.*, 2005, **152**, J23–J26.
- S. De, J. Zhang, R. Luque and N. Yan, *Energy Environ. Sci.*, 2016, **9**, 3314–3347.
- A. Roy, M. R. Talarposhti, S. J. Normile, I. V. Zenyuk, V. De Andrade, K. Artyushkova, A. Serov and P. Atanassov, *Sustainable Energy Fuels*, 2018, **2**, 2268–2275.
- W. Sheng, A. P. Bivens, M. Myint, Z. Zhuang, R. V. Forest, Q. Fang, J. G. Chen and Y. Yan, *Energy Environ. Sci.*, 2014, **7**, 1719–1724.
- S. Lu, J. Pan, A. Huang, L. Zhuang and J. Lu, *Proc. Natl. Acad. Sci. U. S. A.*, 2008, **105**, 20611–20614.
- S. Kabir, K. Lemire, K. Artyushkova, A. Roy, M. Odgaard, D. Schlueter, A. Oshchepkov, A. Bonnefont, E. Savinova, D. C. Sabarirajan, P. Mandal, E. J. Crumlin, I. V. Zenyuk, P. Atanassov and A. Serov, *J. Mater. Chem. A*, 2017, **5**, 24433–24443.
- Z. Zhuang, S. A. Giles, J. Zheng, G. R. Jenness, S. Caratzoulas, D. G. Vlachos and Y. Yan, *Nat. Commun.*, 2016, **7**, 10141.
- A. Alowasheer, S. Tominaka, Y. Ide, Y. Yamauchi and Y. Matsushita, *CrystEngComm*, 2018, **20**, 6713–6720.
- Q. Liu, L. Xie, F. Qu, Z. Liu, G. Du, A. M. Asiri and X. Sun, *Inorg. Chem. Front.*, 2017, **4**, 1120–1124.
- Y. Wang, L. Chen, X. Yu, Y. Wang and G. Zheng, *Adv. Energy Mater.*, 2017, **7**, 1601390.
- K. Xu, P. Chen, X. Li, Y. Tong, H. Ding, X. Wu, W. Chu, Z. Peng, C. Wu and Y. Xie, *J. Am. Chem. Soc.*, 2015, **137**, 4119–4125.
- P. Hou, X. Wang, Z. Wang and P. Kang, *ACS Appl. Mater. Interfaces*, 2018, **10**, 38024–38031.
- L. Gao, Y. Wang, H. Li, Q. Li, N. Ta, L. Zhuang, Q. Fu and X. Bao, *Chem. Sci.*, 2017, **8**, 5728–5734.
- A. G. Oshchepkov, A. Bonnefont, S. N. Pronkin, O. V. Cherstiov, C. Ulhaq-Bouillet, V. Papaefthimiou, V. N. Parmon and E. R. Savinova, *J. Power Sources*, 2018, **402**, 447–452.
- W. Ni, A. Krammer, C.-S. Hsu, H. M. Chen, A. Schüller and X. Hu, *Angew. Chem., Int. Ed.*, 2019, **58**, 7445–7449.
- O. V. Cherstiov, P. A. Simonov, A. G. Oshchepkov, V. I. Zaikovskii, T. Y. Kardash, A. Bonnefont, V. N. Parmon and E. R. Savinova, *J. Electroanal. Chem.*, 2016, **783**, 146–151.
- D. A. Tryk, G. Shi, H. Yano, J. Inukai, H. Uchida, A. Iiyama, M. Matsumoto, H. Tanida, M. Arao and H. Imai, *ECS Trans.*, 2018, **85**, 41–46.

- 32 D. Wang, C. V. Subban, H. Wang, E. Rus, F. J. DiSalvo and H. D. Abruña, *J. Am. Chem. Soc.*, 2010, **132**, 10218–10220.
- 33 J. H. Wee and K. Y. Lee, *J. Power Sources*, 2006, **157**, 128–135.
- 34 C. Zhu, A.-L. Wang, W. Xiao, D. Chao, X. Zhang, N. H. Tiep, S. Chen, J. Kang, X. Wang, J. Ding, J. Wang, H. Zhang and H. J. Fan, *Adv. Mater.*, 2018, **30**, 1705516.
- 35 M. Ledendecker, S. Krick Calderón, C. Papp, H. P. Steinrück, M. Antonietti and M. Shalom, *Angew. Chem., Int. Ed.*, 2015, **54**, 12361–12365.
- 36 Y. Gu, S. Chen, J. Ren, Y. A. Jia, C. Chen, S. Komarneni, D. Yang and X. Yao, *ACS Nano*, 2018, **12**, 245–253.
- 37 D. Strmcnik, M. Uchimura, C. Wang, R. Subbaraman, N. Danilovic, D. van der Vliet, A. P. Paulikas, V. R. Stamenkovic and N. M. Markovic, *Nat. Chem.*, 2013, **5**, 300–306.
- 38 N. Danilovic, R. Subbaraman, D. Strmcnik, K. C. Chang, A. P. Paulikas, V. R. Stamenkovic and N. M. Markovic, *Angew. Chem., Int. Ed.*, 2012, **51**, 12495–12498.